Agricultural and Forest Meteorology 249 (2018) 187–197

Contents lists available at ScienceDirect

Agricultural and Forest Meteorology

journal homepage: www.elsevier.com/locate/agrformet

Measured and modelled wind variation over irregularly undulating terrain

John D. Wilson

Department of Earth & Atmospheric Sciences, University of Alberta, Edmonton, Canada

ARTICLE INFO

Keywords:
Disturbed surface layer winds
Inverse dispersion
Micrometeorology
Site characterization
Wind model

ABSTRACT

The steady-state, Reynolds-averaged momentum equations, with a simple eddy viscosity closure, are solved numerically to compute the spatial variation in surface-layer mean windspeed over irregular, gently rolling terrain. Simulations, with both this non-linear model "ASL3D" and (for comparison) with the pre-existing linear "Mixed Spectral Finite-Difference" or MSFD model, are compared with observed winds from anemometers aligned on a 140 m transect in a rolling field near Lacombe, Alberta. Recorded wind speeds, normalized and aggregated by wind direction sector, characterize local wind variation over terrain whose elevation varied by roughly ± 10 m over a radius of about half a kilometer from the instrumented transect.

For northeast and southwest winds particularly, both models agree well with the observations. In southeast winds, observed spatial variation of the wind was weak, except that an anemometer close to fences and gates recorded distinctly lower speeds: provided those obstructions are represented by adding a localized sink in the momentum equations, the ASL3D model transect is (again) in quite good agreement with the observations. For northwest winds, however, agreement of modelled and measured transects is poor, presumably because a steep, wooded slope lay upwind from the anemometer array. Overall the linear correlation coefficient between modelled and observed *fractional deviations* of wind speed from the reference value is 0.72.

Other than as regards the flexibility to represent such complications as fences, plant canopies (etc.), computed wind fields over for the present terrain do not suggest any compelling advantage of the more laborious non-linear model (ASL3D) over the semi-analytical MSFD treatment. It is concluded that, when applied over gentle terrain, the skill intrinsic to even such a simple paradigm as ASL3D (and MSFD) represents a meaningful and potentially useful alternative to the neglect of lateral inhomogeneity.

1. Introduction

The supposition that velocity (and other) statistics are invariant on horizontal planes underlies many or even most practical applications of surface layer meteorological theory, but most experimentalists will have faced the conundrum of an imperfect field site at which one is obliged – or in the interests of simplicity, one chooses – to overlook lateral inhomogeneity, and take wind and turbulence measurements at a single point as being sufficient, courtesy of Monin–Obukhov similarity theory (MOST), to characterise overall site conditions. An example relevant to this paper is the trace gas experiment of Hu et al. (2016), performed on hilly land: though it was known (and acknowledged) to be untrue, their Lagrangian stochastic inverse dispersion calculations treated wind statistics as if they had been laterally uniform, when "seen" in a terrain-following coordinate.

The approximation invoked by Hu et al. proved adequate and their "bLS" (backward Lagrangian stochastic) inversion method robust, but there are liable to be circumstances where accounting for the impact on wind statistics of varying topography and/or cover is worthwhile — even if doing so mandates that one resort to an onerous wind calculation. Taking inverse dispersion as case in point, wherever concentration measurements are made very close to a source a Lagrangian (i.e. trajectory simulation) treatment to determine emission rate is preferred, because the Eulerian description misrepresents the non-diffusive near field of a source (e.g. Raupach, 1989). In this context the role, potentially, of a wind model, would be to provide three-dimensional fields of mean velocity, Reynolds stress and turbulent kinetic energy (TKE) dissipation rate to a suitable LS trajectory model (e.g. Thomson, 1987; Wilson et al., 2010).

It is broadly in the above context then — the micrometeorology of mildly non-uniform sites — that this paper will explore the utility of numerical fluid mechanics in almost its simplest form: the steady-state, Reynolds-averaged momentum equations, with eddy viscosity closure, are solved for the situation where irregular terrain undulations cause wind variations that could be said to occur on the surface layer scale. The approach taken (Fig. 1) is to adopt a laterally periodic computational flow domain. This obviates the need to provide a known upwind profile of flow statistics; and if those lateral boundaries are placed

E-mail address: jaydee.uu@ualberta.ca.

https://doi.org/10.1016/j.agrformet.2017.11.026
Received 13 June 2017; Received in revised form 3 October 2017; Accepted 21 November 2017

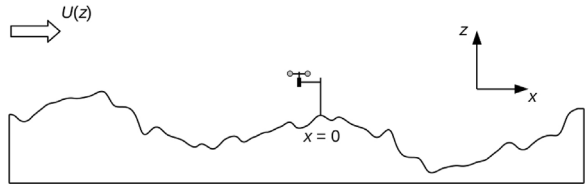

Fig. 1. A complicated field site where wind statistics are horizontally (as well as vertically) inhomogeneous, such that it is nowhere plausible that Monin–Obukhov similarity theory correctly describes wind statistics in the atmospheric surface layer (ASL). The approach used here to describe the wind field is to compute its structure within a laterally periodic domain centered over the region of interest, and rescale modelled wind statistics to match the measurements made at a single point. It is assumed that the wind is practically uniform, at the top of the atmospheric surface layer ("ASL").

sufficiently far from the area over which it is of interest to evaluate the wind statistics, the influence of the distant terrain ought to be weak. The calculation is driven by an imposed shear stress (or an imposed horizontal velocity) far overhead, and computed velocity statistics are re-scaled so that they match experimental input *at a single point in the flow*.

A brief overview on boundary layer wind models is in order (for detailed reviews see, e.g., Hunt, 1980; Taylor et al., 1987; Finnigan, 1988; Carruthers and Hunt, 1990; Wood, 2000). By carrying out a perturbation analysis (linearising the governing equations by an expansion in powers of small parameters) Jackson and Hunt (1975 showed that variation of the wind blowing over a smooth ridge could be regarded as being "driven" by a streamwise pressure gradient that could be obtained by solving for the velocity field in an irrotational (non-turbulent) "outer layer", the Fourier transform of the perturbation pressure field being determined by the Fourier transform of the hill profile. Below the outer layer a turbulent inner layer is perturbed by this imposed pressure field, and its response is modulated by a shear stress field that, for the geometry considered, is adequately treated in terms of a Prandtl eddy viscosity with an undisturbed turbulence length scale (, where k_v is the von Karman constant and η the distance from ground). Furthermore although the validity of the JH75 analysis hinged on stringent restriction of the geometry (i.e. hill slope and other dimensionless factors) the solution, generalised to three dimensional terrain by Mason and Sykes (1979, has been found useful to predict the changes in mean windspeed above topography that in fact violates those restrictions. Wind models — including the JH75/MS79 model, a family of less restrictive linear models (notably the "Mixed Spectral Finite-Difference" model MSFD originated by Beljaars et al., 1987a, and briefly described in Appendix A), and numeric, non-linear simulations (e.g. Taylor, 1977a, Taylor, 1977b; Zeman and Jensen, 1987; Raithby et al., 1987) — have been tested against wind tunnel (e.g. Britter et al., 1981) or field measurements of winds over a number of more or less isolated hills, the early studies including Kettles Hill (Taylor et al., 1983b), Ailsa Craig (Jenkins et al., 1981), Askervein (Castro et al., 2003; Golaz et al., 2009) and Brent Knoll (Mason and Sykes, 1979). Experience suggests that eddy viscosity closure is adequate for prediction of the mean wind field over gently sloping terrain (e.g. Ayotte et al., 1994; Ying et al., 1994), but that a more sophisticated turbulence closure is demanded to realistically model spatial variation of turbulence statistics.

Returning to the goal (here) of modelling wind over terrain whose elevation changes are relatively insignificant — at least compared to the above named test sites, and the sort of topography of interest in regard to wind energy resources — there is no reason to suppose that an approach well proven for terrain the amplitude of whose elevation is of order 100–1000 m should not be equally (or even more) satisfactory for much lower terrain. However the above studies generally focused on one relatively isolated and dominant terrain feature (hill or ridge), whereas this study addresses the case where there is no dominant topographic feature. As a consequence it is less clear what should constitute an adequate domain size, and whether available topographic data will offer adequate resolution.

Section 2 outlines the numerical wind model whose performance is tested here (for convenience of reference, "ASL3D"), while Appendix A briefly describes the linearized MSFD model to which (apart from the linearization) it is closely matched. Section 3 tests the performance of ASL3D in idealized, previously studied flows; and Section 4 compares simulations (ASL3D & MSFD) with near-ground wind measurements over irregular, rolling pasture.

2. Numerical model: ASL3D

The objective here is to model variation of the surface layer wind over horizontal distances spanning of the order of a few hundred metres, in response to disturbance by smooth and gentle terrain whose height $h = h(x, y)$ varies by an amount of the order of 10 m. Tacitly excluding application to any case of very light winds — such cases anyway having been excluded from the data used here to test the model — it seemed not unreasonable to treat the (model) atmosphere as being unstratified (i.e. uniform in its mean potential temperature), and to consider the topographic disturbance to the wind as taking place within a "host" (i.e. background) flow that could be approximated as being a constant stress layer.[1] Support for the latter simplification can be found in Taylor (1977a, Table II), where his comparison of "surface layer" versus "PBL" model results for the pressure and shear stress deviations over a Gaussian hill indicates them to be consistent, to within about 10%.

The mean momentum equations and the turbulent kinetic energy (TKE) equation were transformed into a terrain following coordinate

$$\eta = H\,\frac{z-h}{H-h} \tag{1}$$

where H is the computational domain depth: on ground the absolute elevation is $z = h(x, y)$, whereas $\eta = 0$. The resulting equations were closed using an eddy viscosity $K = \lambda\sqrt{c_e E}$, where E is the turbulent kinetic energy and λ a prescribed turbulence length scale, and after elimination of terms considered unimportant they were solved numerically using periodic lateral boundary conditions. The widely used control volume method "SIMPLEC" (van Doormaal and Raithby, 1984; Patankar, 1980) was adopted, along the lines explored earlier (Wilson, 1985, 2004b) for windbreak flows. Details follow.

2.1. Governing equations

Let (u, v, w) be the local, instantaneous, Cartesian velocity components, U (etc.) the mean velocities and u' (etc.) the velocity fluctuations defined by the Reynolds decomposition $u = U + u'$. Upon transformation of the Navier–Stokes equations into the non-orthogonal (x, y, η)-coordinate system it is convenient to introduce an effective vertical velocity

$$w^* \equiv u\eta_x + v\eta_y + w\eta_z \tag{2}$$

such that (u, v, w^*) is non-divergent in $x - y - \eta$ space, i.e.

$$\frac{\partial u}{\partial x} + \frac{\partial v}{\partial y} + \frac{\partial w^*}{\partial \eta} = 0\ , \tag{3}$$

and with the result that vertical advection terms take the form $w^*\partial/\partial\eta$ (e.g. Richards and Taylor, 1981; Doyle et al., 2013). After Reynolds averaging, adoption of an eddy viscosity closure, and the simplification or neglect of certain minor terms, the following approximate mean momentum equations result:

[1] The generalization to provide a full boundary layer (with Coriolis forces) as host flow is straightforward.

$$\frac{\partial}{\partial x}\left(\mathrm{UU} - K_a\frac{\partial U}{\partial x}\right) + \frac{\partial}{\partial y}\left(\mathrm{VU} - K_a\frac{\partial U}{\partial y}\right) + \frac{\partial}{\partial \eta}\left(W^* U - \eta_z^2 K\frac{\partial U}{\partial \eta}\right) = -\frac{\partial P}{\partial x} - \eta_x\frac{\partial P}{\partial \eta}, \quad (4)$$

$$\frac{\partial}{\partial x}\left(\mathrm{UV} - K_a\frac{\partial V}{\partial x}\right) + \frac{\partial}{\partial y}\left(\mathrm{VV} - K_a\frac{\partial V}{\partial y}\right) + \frac{\partial}{\partial \eta}\left(W^* V - \eta_z^2 K\frac{\partial V}{\partial \eta}\right) = -\frac{\partial P}{\partial y} - \eta_y\frac{\partial P}{\partial \eta}, \quad (5)$$

$$\frac{\partial}{\partial x}\left(\mathrm{UW} - K_a\frac{\partial W}{\partial x}\right) + \frac{\partial}{\partial y}\left(\mathrm{VW} - K_a\frac{\partial W}{\partial y}\right) + \frac{\partial}{\partial \eta}\left(W^* W - K_a\frac{\partial W}{\partial \eta}\right) = -\eta_z\frac{\partial P}{\partial \eta}. \quad (6)$$

Though this framework is by no means new, a brief interpretation may be warranted. The principle here has been to retain what are presumably the dominant terms, viz., advection, shear stress gradients, and (kinematic) pressure gradients (note: Eqs. 3–6 hinge on adopting the Boussinesq approximation, and P is the mean deviation of the kinematic pressure from a hydrostatic reference state, i.e. the pressure *disturbance* induced by the topography). Coriolis terms have been discarded, as the time scale for advection across the domain is on the order of minutes; so, too, have been all the "cross" diffusion terms that would arise from the mechanical imposition of an eddy viscosity closure having the proper tensor symmetry. Because the diagonal elements of the Reynolds stress tensor cannot be realistically modelled under eddy viscosity closure and (anyway) their gradients are usually judged less important than those of the shear stresses, a distinction has been made here between the "real" eddy viscosity K, and an artificial eddy viscosity K_a that, though required to be small with respect to K, is nevertheless retained as potentially useful in terms of numerical stability, and wherever K_a *should* appear multiplied by η_z (which, note, is independent of η) that factor has been eliminated as inessential. Conversely, it is easy to show that the η_z^2 factor must be retained if the important shear stress gradients $\partial(\overline{u'w'}, \overline{v'w'})/\partial z$ are to be correctly treated. (Distinct values K_a^h, K_a^v for the artificial viscosity as applied to horizontal and vertical diffusion were applied, with $K_a^v = 0.001\ \mathrm{m^2\,s^{-1}}$ and $K_a^h = 0.1\ \mathrm{m^2\,s^{-1}}$, but for clarity of notation the distinction is suppressed above.)

Completing the above dynamical model, the eddy viscosity $K = \lambda\sqrt{c_e E}$ has been constructed from an algebraic length scale whose inverse is

$$\frac{1}{\lambda} = \frac{1}{k_v\eta} + \frac{1}{\lambda_0}, \quad (7)$$

(λ_0 being an imposed upper limit to the lengthscale) and a simplified turbulent kinetic energy (TKE) equation

$$\frac{\partial}{\partial x}\left(\mathrm{UE} - K_a\frac{\partial E}{\partial x}\right) + \frac{\partial}{\partial y}\left(\mathrm{VE} - K_a\frac{\partial E}{\partial y}\right) + \frac{\partial}{\partial \eta}\left(W^* E - \eta_z^2 K\frac{\partial E}{\partial \eta}\right) = K\left[\left(\eta_z\frac{\partial U}{\partial \eta}\right)^2 + \left(\eta_z\frac{\partial V}{\partial \eta}\right)^2\right] - \frac{(c_e E)^{3/2}}{\lambda}. \quad (8)$$

Again, in Eq. (8) a plethora of minor terms have been dropped in favour of simplicity.

2.2. Grid and discretization

Nodes of the computational grid (Fig. 2) are indexed (i, j, k) along respectively the (x, y, η) axes, the horizontal coordinate x increasing towards the east, and y towards north. Mean velocity nodes were offset relative to the pressure nodes, with turbulent kinetic energy nodes chosen to coincide with the latter; in terms of their vertical location, nodes for U, V, P were placed midway between the W nodes. Vertical velocity nodes were placed on ground (i.e. at $\eta = z_0$, the surface roughness length) and on the bounding upper plane ($\eta = H$) of the computational domain.

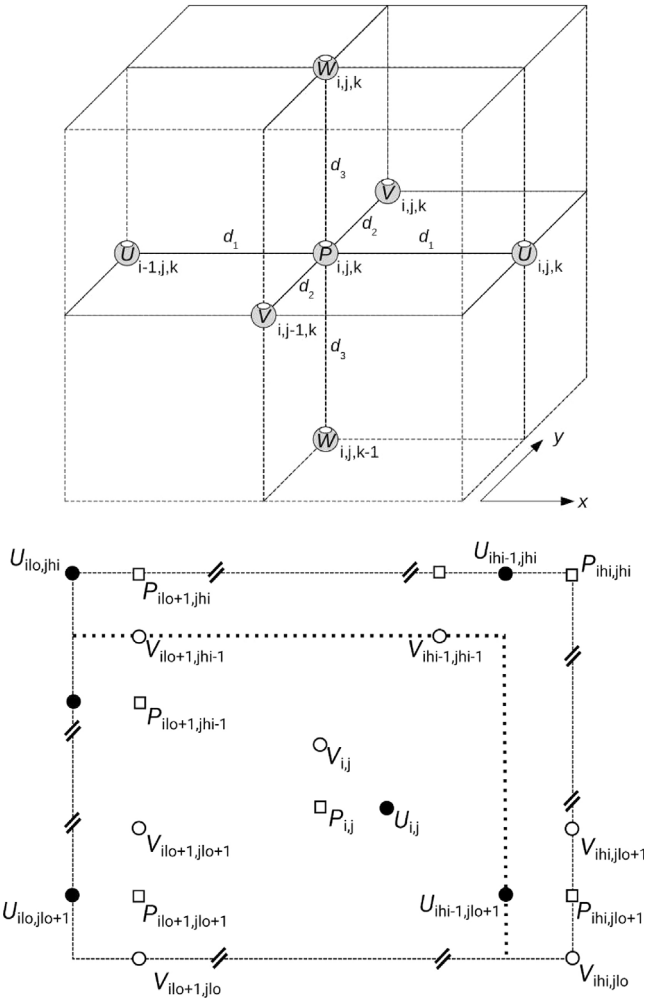

Fig. 2. Upper: staggered grid points centred around a P node. Lower: domain and mesh, seen from above (W-nodes, which are above and therefore project onto P nodes, are not shown). The outer rectangle embraces all active nodes used with periodic lateral boundary conditions.

The western boundary of the domain ran through U nodes (indexed $U(ilo, j, k)$) and the southern boundary through V nodes (indexed $V(i, jlo, k)$); eastern and northern boundary planes ran through P (and therefore W) nodes. Implementing periodicity was a simple matter of care with the indexing of "neighbour" nodes. The net (convective plus diffusive) flux across each control volume face was approximated (as a function of the Peclet number) in terms of the bracketing gridpoint values of velocity (and the transported entity), using Patankar's (1980) power law scheme.

2.3. Boundary conditions on the ground and at the upper surface

The upper boundary of the computational domain at $\eta = H$ is a flat surface both in (x, y, η)-space and in real space. By assumption, the turbulent shear stresses driving the flow are constant on that plane, and (in view of the positioning of the horizontal velocity nodes) serve as the needed upper boundary conditions for the uppermost (U, V) control volumes. On $\eta = H$, it is assumed that vertical velocity $W = 0$ (from which it follows also that $W^* = 0$); simulations that instead imposed $\partial W^*/\partial\eta = 0$ on $\eta = H$ proved indistinguishable on all domains for which the alternatives were both tested.

Now as regards the lower boundary conditions, whereas W nodes fall on ground (thus $W = 0$) it is necessary to prescribe the exiting momentum fluxes to ground from the lowest plane of U- and V-nodes. Let (U_P, V_P) designate the velocity components at those nodes (height η_P

above terrain). Assuming an equilibrium layer extends to this height, the surface drag was evaluated as (e.g. taking the x-component)

$$\overline{u'w'}^{(0)} = -C_D U_P \sqrt{U_P^2 + V_P^2}\,, \tag{9}$$

where the drag coefficient

$$C_D = \left(\frac{k_v}{\ln(\eta_P/z_0)}\right)^2 \tag{10}$$

is that implied by a rearrangement of an (assumed) shallow semi-logarithmic wind profile extending over $z_0 \le \eta \le \eta_P$. To ensure that the drag will oppose whatever may prove to be the next, i.e. $(m+1)$th, guess for the component U_P^{m+1} it is necessary to linearise this expression, based on the known (U_P^m, V_P^m) of the completed prior (mth) iteration. An adequate factorization, used for most simulations, is

$$\overline{u'w'}^{(0)} = -C_D U_P^{m+1} \sqrt{(U_P^m)^2 + (V_P^m)^2} \tag{11}$$

(in terms of speed of convergence, no advantage followed from a rigorous linearization using the tangent $\partial\overline{u'w'}^{(0)}/\partial U_P$). Finally, the condition $\partial E/\partial\eta = 0$ was imposed on TKE at both lower and upper boundaries.

2.4. Closure constants

The closure constant c_e (appearing in the eddy viscosity $K = \lambda\sqrt{c_e E}$ and in the TKE dissipation term of Eq. (8)) is chosen in reference to an ideal neutral constant stress layer in local equilibrium, in order to ensure that the product $c_e E$ equates to the magnitude (u_*^2) of the vertical momentum flux. This ensures that (for the reference flow) TKE production $-\overline{u'w'}\,\partial U/\partial z \equiv u_*^3/\lambda$ exactly balances TKE dissipation $(c_e E)^{3/2}/\lambda$, where (for the purposes of the calibration) $\lambda = k_v z$. For the calculations below it was assumed that $c_e^{-1} \equiv E/u_*^2 = 4.8$ (corresponding to the supposition that in undisturbed, neutrally stratified surface layer flow the normalized velocity standard deviations $\sigma_u/u_* = \sigma_v/u_* = 2$, $\sigma_w/u_* = 1.3$).

Simulations were not very sensitive to the value of the limiting length scale λ_0 in Eq. (7), and for the results shown $\lambda_0 = 200$ m.

2.5. Matrix inversions

When integrated over their control volumes, the mean momentum equations give rise to linear algebraic "neighbour equations" that interrelate (say) U^{m+1}, the sought-for next guess (labelled guess "$m+1$") for the velocity component U at some arbitrary node, to its (up to) six nearest neighbours on the grid; taking UU as an example of a non-linear term, linearization is accomplished (without loss of accuracy) by representing this as the product $U^m U^{m+1}$ of successive estimates labelled m, $m+1$ (after many iterations, the two estimates converge).

For any one (sought for) field, say U^{m+1}, and with all others for the moment fixed, one solves by iterating a "line-by-line solver". Because of the lateral periodicity of the domain, in general the matrix of neighbour coefficients requiring to be inverted is not tridiagonal, due to there being non-zero coefficients at upper right and lower left ("cyclic tridiagonal system"). The Numerical Recipes subroutine "cyclic" was exploited. Interested readers may refer to Patankar (1980), Versteeg and Malalasekera (1995), and Ferziger and Perić (1997) for related details of numerical procedure.

2.6. Criterion for cessation of iterations

In view of the periodic lateral boundary conditions, there can be no net flow of momentum across the side boundaries of the domain. Therefore if the integral (whole domain) momentum budget is to be satisfactory, the area-integrated U-momentum flux

$$I_U(H) \equiv -\iint_{\mathscr{A}} \overline{u'w'}(x, y, H)\,\mathrm{d}x\,\mathrm{d}y \tag{12}$$

imposed at the upper boundary $\eta = H$ must match the sum of (i) the corresponding area-integrated momentum flux $I_U(0)$ to ground, plus (ii) the area-integral D_x of form drag on terrain. The criterion for cessation of iterations was that the (fractional) imbalance

$$\delta_U \equiv \left|\frac{I_U(\eta_{mx}) - I_U(0) - D_x}{I_U(\eta_{mx})}\right| \tag{13}$$

in the whole domain U momentum budget be small (for solutions shown below, 3% or smaller).

3. Testing ASL3D for simple flows

ASL3D was coded in Fortran-90 and compiled on Linux machines (including a laptop) using standard gcc-fortran. This section documents cautionary steps taken to establish that the new code correctly solves the coupled equations constituting the wind model.

The first such step was to ascertain that the subroutines that *solve* the (discretized) partial differential equations would perform as required: confirmation is provided by Appendix B. Next in terms of primacy was to check that in the *absence* of any mechanism (such as topography) that might disturb the surface layer flow, the model should alight upon (or *preserve*) a realistic equilibrium solution across the entire lateral span of its domain.

The equilibrium (i.e. no terrain) solution was computed from the reduced governing equations (in which all horizontal derivatives vanish). As necessitated by the form of the equations in the limit $\partial/\partial x = \partial/\partial y = 0$, the shear stress was height independent and the mean wind profile (correctly) logarithmic near ground, but not quite so aloft due to the imposed limitation on the growth of the length scale. The TKE profile, too, was close to height-independent. Similar equilibrium solutions (similar closure, similar numerical methodology) have been quantitatively compared with field and wind tunnel observations by Wilson et al. (1998). In short, the equilibrium solution gives a realistic representation of the mean wind, shear stress and TKE fields of the ideal, undisturbed ASL.

The equilibrium solution provides a convenient initial guess for the 3D fields[2] (of U, V, E). With the terrain suppressed and the program forced to iterate, those initial fields ("$U_0(\eta)$", etc.) ideally should be perfectly preserved across the domain. When that test was performed on a 1 km × 1 km domain (with $\Delta x = \Delta y = 10$ m), after more than 1000 'outer' iterations ($m \to m+1$) the initial fields had been preserved to within 1 part in 10^4. Such small degradation of the solution as did occur can be attributed to the immensely more numerous calculations underpinning the 3D calculation than the equilibrium calculation, and the attendant roundoff errors.

3.1. Sinusoidal lower boundary

Because it is a case investigated by earlier authors (e.g. Taylor et al., 1983a; Taylor, 1998; Weng et al., 2000), the model flow's response when perturbed by an infinite sequence of sinusoidal ridges provided a useful test. The kinematic shear stress vector at the top boundary was prescribed so as to direct the flow along the x-axis, and surface topography was specified as $h(x, y) = h_0[1 + \cos(k x)]/2$, where h_0 is the trough-to-peak height difference and $k = 2\pi/\lambda$ the terrain wavenumber. Solutions were computed with one full topographic wave along the computational domain, the latter covering $-352.5 \le x \le 352.5$ m along the x-axis (specifically, xw(ihi) + Δx/2 − xu(ilo) = λ = 705 m), ± 50 m along the transverse (y) axis, and having a depth of 500 m. The roughness length was specified $z_0 = 0.0705$ m

[2] This is in some sense an illusory role: lateral periodicity of the domain obviates any need for inflow profiles, so that apart from questions of numerical stability, *any* set of initial 3D fields could be chosen. The 3D solution, as noted above, is driven purely by the specified shear stresses $\overline{u'w'}$, $\overline{v'w'}$ at the top of the flow domain, whose relative values determine the wind direction aloft.

such that $\lambda/z_0 = 10^4$, and the "hill height" h_0 was adjusted to control the maximum slope $\alpha \equiv k\,h_0/2$ of the topographic wave, for comparability with earlier studies. Horizontal resolution was $\Delta x = \Delta y = 5$ m; vertical resolution was a constant $\Delta\eta = 0.05$ m below $\eta = 1$ m, but was progressively stretched above $\eta = 1$ m (by 20% in each successive layer) to a maximum value of $\Delta\eta = 30$ m.

For wind models both linear and non-linear, and as a function of the (maximum) terrain slope, Taylor's (1998, Fig. 6a) gives the computed fractional increase in mean wind speed at the crest of the sinusoidal ridge "relative to the flow over a flat surface", viz.

$$\Delta S_{\max} = \frac{U(x_c, \eta) - U_0(\eta)}{U_0(\eta)} ,$$

where x_c (=0) denotes the position of the ridge crest, η ($\approx 100\, z_0$ here) the height above ground, and $U_0(\eta)$ the wind speed over a flat surface (for the same applied shear stress at the upper boundary). When the maximum slope was specified as $\alpha = 0.2$ the present model ASL3D yielded $\Delta S_{\max} = 0.31$, which is exactly consistent with the value cited by Taylor for a variant ("NLMSFD") of MSFD that retains the non-linear advection terms (whereas for the linear MSFD, $\Delta S_{\max} \approx 0.46$).

3.2. Windbreak flow

A second preliminary test of the code placed an infinitely long porous windbreak fence (height $h_f = 2$ m, resistance coefficient $k_r = 2$) along the y-axis at $x = 0$, with the mean flow directed along the x-axis. The terrain was flat, with roughness length $z_0 = 0.01$ m. To parameterize the windbreak, a momentum sink

$$S_u = -k_r\, U \sqrt{U^2 + V^2}\, \delta(x - 0)\, s(\eta - h_f) \tag{14}$$

was inserted on the right hand side of Eq. (4), where $\delta(\cdot)$ is the "delta-function" (unit: m^{-1}) and $s(\cdot)$ is a dimensionless step function (the $\delta \times s$ factor localizes drag to occur only "at" the fences; only control volumes whose upper boundary is at or below $\eta = h_f$ and that span the fence "experience" the drag force).

A simulation was performed over a domain spanning ± 100 m in the streamwise direction and ± 10 m laterally, with horizontal grid-lengths $\Delta x = \Delta y = 0.5$ m. The domain depth was $H = 50$ m; vertical resolution was a uniform $\Delta\eta = 2z_0$ below $\eta = 0.5$ m, and was stretched progressively (by 20% for each successive layer) to a maximum value of 5 m. The computed transect of relative windspeed along $z/h_f = 1/2$ exhibited a minimum value of $U/U_0 = 0.44$ downwind of the windbreak at $x/h_f = 1.5$, an outcome that concurs well with the expected minimum value

$$\frac{U}{U_0} = 1 - \frac{k_r}{(1 + 2k_r)^{0.8}} = 0.45 \tag{15}$$

(Wilson et al., 1990) for an isolated windbreak with the same specifications; the location of the computed velocity minimum was consistent with Wilson's (1985, Fig. 7) results for eddy viscosity closures.

4. Comparison of simulations with measured winds over undulating terrain

During August 2013 mean wind speeds were measured (at height $z = 1.12$ m) over gently rolling pasture in central Alberta, sampling an area of roughly 20 m × 140 m within "plot 22" at the Lacombe Research Centre of Agriculture and Agri-Food Canada (52.457393 N, 113.765297 W). The topography and instrument layout at the site are indicated by Figs. 3 and 4 (see also Hu et al., 2016). The mean wind direction β from a wind vane was assumed to characterize the overall orientation of the flow, and that signal was very consistent with the mean wind direction from a (temporarily) nearby 3-dimensional sonic anemometer (Campbell Scientific CSAT3).

Repeated experience (in the wind tunnel and in the field) has proven the cup anemometers that were used (Climet, Inc., 011-4) to be highly inter-consistent, provided mean windspeeds are higher than about 1 m s^{-1} (e.g. Wilson, 2004a, Table II). All signals were recorded on Campbell Scientific dataloggers, and organised into 15-min averaging intervals. The individual fifteen minute mean speeds (S) were normalized relative to the value (S_{ref}) at one location, the reference anemometer (see Fig. 4), and – excluding intervals for which the reference anemometer reported a mean wind speed below a chosen threshold – these normalized mean speeds were binned (averaged) within sectors ($\beta = \beta_0 \pm 22.5^\circ$) of mean wind direction centred on the 8 cardinal directions $\beta_0 = 0, 45, 90, \ldots, 315^\circ$. Hu et al. (2016, Fig. 3) presented the mean wind rose for several of the anemometers, the range in relative mean wind speed spanning $0.85 \le S/S_{\mathrm{ref}} \le 1.05$.

Unless otherwise stated, for the measured wind transects to be shown below, the threshold wind speed has been set at

Fig. 3. "Plot 22" at Lacombe, looking towards the north from the southern boundary fence. The origin of the coordinate system lies at the junction of the two visible fences, just out of sight at the lower left of the photograph. The distance along the western fence from the origin to the gate on the skyline is 290 m. Note the cup anemometers, and a single sonic anemometer at the right of the photo.

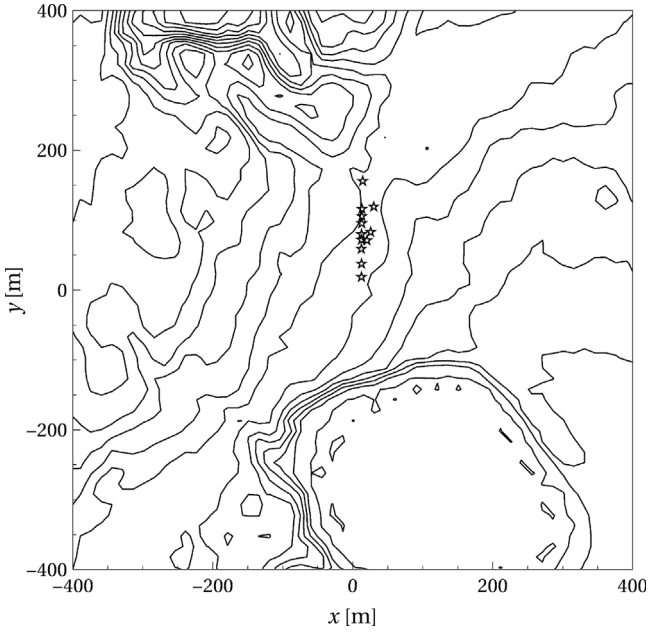

Fig. 4. Terrain contours (interval 2 m) and positions of cup anemometers (stars). Coordinates of the southernmost anemometer are $(x, y) = (12.4, 18.7)$ m. Note the steep descent to a small lake south of the anemometers, and a steep slope seen at the upper left (northwest of the anemometers). The reference anemometer is the third from the south end of the transect along $x = 12.4$ m, its coordinates being $(x, y) = (12.3, 59)$ m. Anemometer no. 9 is at the north end of the transect, in a narrow gulley.

$S_{ref}^{min} = 2.5\ m\ s^{-1}$. However the measured speed transects proved little different in character with a stricter criterion $S_{ref}^{min} = 4.0\ m\ s^{-1}$, as demonstrated below (Fig. 10). The roughness length for simulations, deduced from the sonic anemometer data, was fixed as $z_0 = 0.08$ m.

4.1. Representation of the terrain in the wind model

According to repeated measurements with a handheld GPS, the UTM (Universal Transverse Mercator) coordinates (easting, northing) of the southwest corner of plot 22 are (12 *U* 0312082 ± 1, 5815335 ± 1), consistent with coordinates from Google Earth with the cursor placed over the image of that spot. Digital elevation files covering the township (TWP 40, ranges 27 and 26 west of the 4th meridian) were purchased from AltaLIS ("LiDAR15 DEM"), in the form of a file organized such that each row gave (x, y, z), with (x, y) being UTM coordinates and z the elevation in metres above sea level given to two decimal places ("Bare Earth XYZ ASCII coordinates"). The horizontal "post" spacing for these data is 15 m (with accuracy 0.5 m), while the cited vertical accuracy is 0.3 m with (an implicit) resolution of the order of 0.01 m. The DEM post closest to the SW corner of plot 22 had coordinates (312082.5, 5815327.5), where each unit increase in the UTM (x or y) coordinate corresponds to a 1 m displacement towards (respectively) the east or the north. A fortran program shifted the coordinate origin such that x, y for each "post" was expressed relative to the SW corner (taken as 312081.5, 5815334.5), and selected an areally square subset of the DEM file centred on the SW corner of plot 22, e.g. $-D_x/2 \le x \le D_x/2$, $-D_y/2 \le y \le D_y/2$ where $D_x = D_y \sim 2000$ m.

The DEM terrain field was interpolated bi-linearly to all horizontally-distinct nodes of ASL3D's computational grid (i.e. *U*, *V* and *P/W/k*), by identifying the four DEM posts surrounding any given node. Linear interpolation has the desirable property that it cannot result in exaggerated terrain slopes when the gridlength is refined to be smaller than the DEM post interval of 15 m.

4.1.1. Terrain filtering

A terrain perturbation height was defined by subtracting the domain-averaged mean elevation from each node's local elevation. Furthermore although only *derivatives* of terrain height appear in the model equations, it was found to be necessary to "taper" the terrain perturbation so as to smoothly vanish at the domain boundaries. This is presumably because lateral periodicity of all model fields had been imposed, and the tapering of (perturbation) elevation has the effect, also, of tapering terrain slope. The terrain perturbation height was attenuated as a function of "excess radius" $r - R$, where $r = \sqrt{x^2 + y^2}$ is the distance from the SW corner of plot 22. Symbolically the damping factor, referred to below as a "Gaussian" filter, was

$$f_d(r; R, \ell_d) = \begin{cases} 1, & r \le R \\ \exp[-(r-R)^2/(2\ell_d^2)], & r > R \end{cases} \quad (16)$$

where R, ℓ_d control the radius of onset and the rapidity of the terrain damping. Typically R, ℓ_d were chosen so that $R + 3\,\ell_d$ would define a circle fitting neatly within the chosen flow domain, ensuring that terrain height and slope would more or less vanish on the domain boundaries.

The above filtering was motivated by the necessity to avoid incurring steep topography near the (periodic) domain boundaries. It was of interest to judge the effect of local terrain smoothing on modelled wind fields, and to that end, for some exploratory runs a further filter was applied: if h represents the "pre-smoothed" terrain height, a weighted mean (i.e. smoothed) height for each gridpoint (i, j) was formed as

$$\tilde{h}_{i,j} = \frac{2}{6} h_{i,j} + \frac{1}{6} [h_{i-1,j} + h_{i+1,j} + h_{i,j-1} + h_{i,j+1}] \quad (17)$$

(i.e. a 1–2–1 filter along each axis).

4.1.2. Model details specific to the Lacombe wind simulations

For the results to be shown, model domain depth was either $H = 960$ m or $H = 480$ m. In either case, below $\eta = 1$ m the height interval between adjacent W nodes (i.e. the vertical gridlength) was uniform and small ($\Delta\eta = 2z_0$), while above 1 m the grid interval was stretched by 20% for each successive cell, to a maximum value (limit). For simulations with domain depth $H = 960$ m, $\Delta\eta^{max} = 50$ m; where $H = 480$ m, $\Delta\eta^{max} = 30$ m.

4.2. Results

Controlling the orientation of the shear stress vector imposed at the top of the domain proved sufficient to ensure that surface wind direction at the model gridpoint closest to the wind vane lay close to the target value, i.e. wind direction varied only very modestly over the entire domain. For a given choice of that vector, the resulting steady state wind speed at any given point (e.g. at the reference anemometer) is dependent on the span of the chosen domain, as well as the manner in which the terrain has been filtered — because the form drag is terrain-specific. This (expected) feature of the simulations is of course obscured when the model windspeeds are normalized so that at the reference anemometer they concur with the observation.

Fig. 5 compares the observed and modeled (ASL3D) windspeed transects for NE winds, giving a broad view of the wind response to topographic features (the case of northeast winds is the most useful, because that wind direction resulted in the most distinct variation of

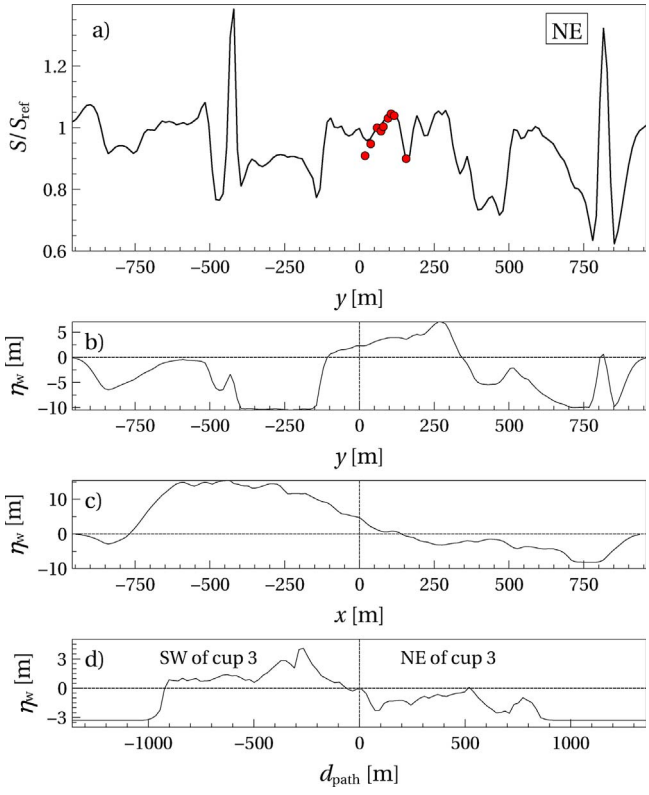

Fig. 5. (a) Observed (filled circles) and modelled (ASL3D, line) transect of relative wind speed for winds from the northeast (NE): (a) transect at $x = 13$ m, encompassing the entire y-axis of the model domain, which spans ± 960 m about the origin on both horizontal axes (horizontal resolution $\Delta x = \Delta y = 12$ m, domain depth $H = 960$ m); (b) filtered terrain perturbation height along the y-axis; (c) terrain height along the x-axis; and (d), *relative* terrain height along a SW–NE line (wind "path") through the reference anemometer (cup no. 3), with negative values lying downwind from cup 3. Terrain is attenuated by the "Gaussian" filter beyond radius $R = 840$ m from the origin, with damping length (or standard deviation) $\ell_d = 40$ m. (The slight SW–NE asymmetry of the manner in which the terrain filter has attenuated the relative terrain transect is explained by the fact that cup no. 3 stood some 60 m north and 13 m east of the coordinate origin.)

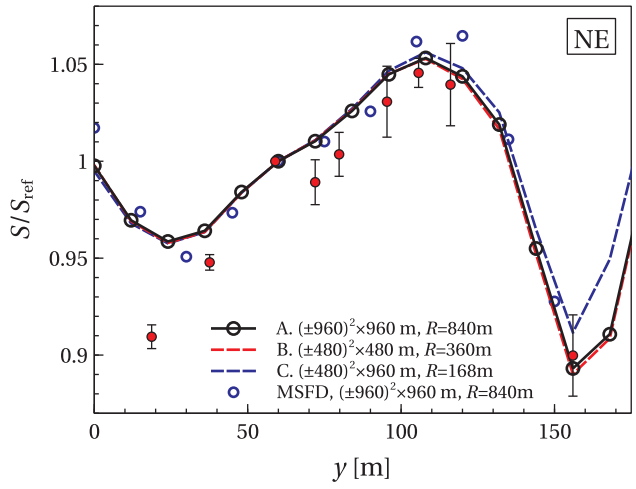

Fig. 6. Sensitivity of ASL3D simulations to domain size and terrain filtering: observed (red-filled circles) and modelled transects of mean wind speed in plot 22 at Lacombe, for NE winds. Error bars on observations give ± standard error. For all simulations, terrain was attenuated beyond the given distance R from the origin, using the Gaussian filter: for ASL3D simulation C, damping length ℓ_d = 24 m, while for all other simulations (both ASL3D and MSFD), ℓ_d = 40 m. For the ASL3D simulations, horizontal resolution $\Delta x = \Delta y$ = 12 m. (For interpretation of the references to color in this figure legend, the reader is referred to the web version of this article.)

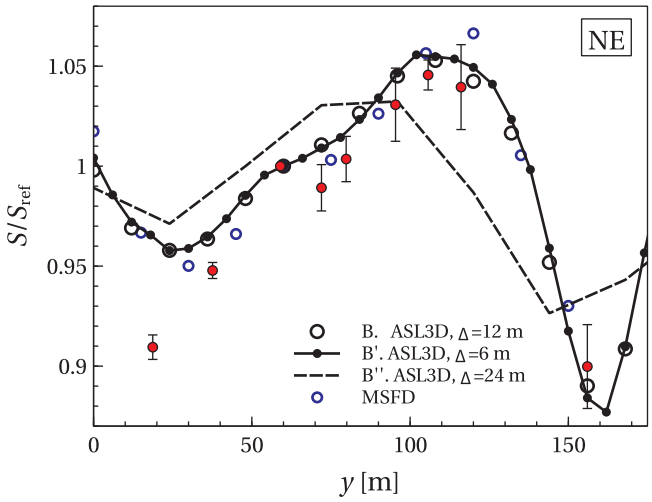

Fig. 7. Sensitivity to horizontal resolution: observed (red-filled circles) and modelled transects of mean wind speed in plot 22 at Lacombe, for NE winds. For all simulations (ASL3D and MSFD) the domain spanned (± 480 × ± 480 × 480 m) along respectively the (x, y, η) axes, and the terrain had been subjected to Gaussian attenuation beyond R = 360 m with damping length ℓ_d = 40 m. ASL3D run B is the same simulation as run B in Fig. 6. (For interpretation of the references to color in this figure legend, the reader is referred to the web version of this article.)

mean wind speed amongst the anemometers). What is evident from Fig. 5, computed with resolution $\Delta x = \Delta y$ = 12 m over a domain spanning ± 960 m about the origin on each horizontal axis, is that the most abrupt spatial gradients in model wind speed align qualitatively with regions of strong topographic slope, as is to be expected.[3] Panels (b, c, d) of Fig. 5 convey the terrain elevation field, which had been subjected to Gaussian attenuation, applied beyond R = 840 m from the origin with standard deviation ℓ_d = 40 m.

Figs. 6 and 7 give a more detailed view of ASL3D simulations for the north-east wind direction, in comparison not only with the measured winds but also with an MSFD calculation (i.e. essentially the linearized equivalent of ASL3D, briefly described in Appendix A). Evidently in terms of domain size and terrain filtering, for present purposes it suffices to ensure that terrain is represented (without attenuation) over a radius of at least about R = 360 m about the origin (run B, domain size $-480 \le (x, y) \le 480$ m with R = 360 m). Quadrupling the area covered by the domain with terrain unattenuated out to R = 840 m (as in run A) produces only a minimal alteration of the solution. It was also found (not shown) that a domain depth of H = 480 m is sufficient, a doubling having no discernable effect over the region of interest.

On the basis of the above finding, it suffices to examine the impact of horizontal resolution on the (± 480 m)^2 domain (Fig. 7). The small difference between ASL3D outcomes with 6 m versus 12 m horizontal resolution establishes that simulations with $\Delta x = \Delta y$ = 12 m are close to being grid-independent, while (unsurprisingly) a coarser simulation with $\Delta x = \Delta y$ = 24 m is much inferior. All told, the strong resemblance of the transect of observed (relative) wind speed to model curves (ASL3D, excepting run B", and MSFD) puts to rest any suspicion that the measured pattern might be without meaning, perhaps a reflection of nothing more than anemometer bias, and beyond causal interpretation.[4] The MSFD solution shown in Fig. 7 differs slightly from that of Fig. 6 as a result of the reduced lateral span of the domain (which results in the terrain being represented by 2^6 = 64 waves rather than 2^7 = 128, for 64 × 15 m gives the domain sidelength 960 m). All in all, the strong similarity of the non-linear and linear (MSFD) solutions testifies to the (expected) adequacy of the linear treatment on this terrain, and lends confidence to the numerical solution (ASL3D). Application of local terrain *smoothing* (as per Eq. (17)) had almost no impact on the model transects.

Fig. 8a compares simulated and observed mean wind speeds for the SW wind direction. Several choices of the computational domain were examined, and as for the case above (i.e. NE winds) it is evident that a domain encompassing about ± 0.5 km (horizontally) relative to the origin and about 0.5 km deep is sufficient (lower domain heights H were not tested). Naturally the computed solution is compromised if the terrain is attenuated *too* close to the region of interest, as clearly shown by ASL3D simulation "D". And regarding terrain attenuation Fig. 8b gives a cross-section along the y-axis of the *unattenuated* terrain perturbation — which is discontinuous across the lateral boundaries and for which (consequently) the ASL3D model failed, i.e. a converged solution could not be obtained — along with examples of the terrain after application of the 'Gaussian' filter that assures the needed upwind/downwind continuity of the imposed terrain field.

Still referring to Fig. 8a and SW winds, the fractional variation in the wind speed is smaller than for the NE case, but once again the correlation of the ASL3D simulations with the observations is striking. At first glance it is not obvious from Fig. 4 why (in this case) the non-linear simulation (ASL3D) should outperform the linear treatment (MSFD), the fetch upwind from plot 22 appearing to be little more complex than it is for NE winds. However there is a sharp gulley some 200 m southwest of plot 22, and the associated steep slope perhaps explains the better simulation by ASL3D. The model transects depart most seriously from observation at anemometer no. 9, the northernmost on the transect, which was positioned in a narrow but distinct gulley (see Fig. 4) that represents the strongest nearby terrain feature. It is not surprising, therefore, that the present simple models (with an imposed turbulence length scale, $\lambda \propto \eta$) should perform poorly in the area of cup no. 9.

For SE winds Fig. 9, observed spatial variation of the mean wind speed was quite modest — if one were to disregard anemometer no. 1 which, at (x, y) = (12.4, 18.7) m, was positioned in the SW corner of

[3] Had the purpose of the anemometers been to test this wind model, they could have been sited so as to sample more dramatic lateral gradients than those across "plot 22" at Lacombe; however the objective was to sample wind variability over the region where trace gas dispersion experiments were ongoing (Hu et al., 2016).

[4] Figs. 6 and 7 show that that anemometer no. 1, at the south end of the transect, lies farthest from the model transect. This low relative wind speed, noted early in the measurement campaign, prompted an exchange of anemometers, but the relative wind speeds at the positions alternately occupied by the two anemometers proved indifferent to the identity of the reporting instrument.

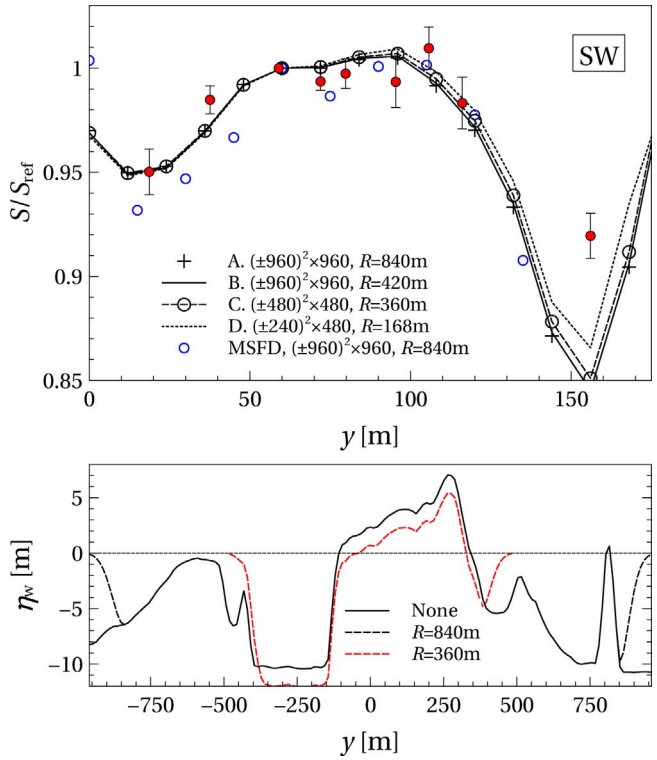

Fig. 8. (a) Observed (filled circles) and modelled transects of mean wind speed in plot 22 at Lacombe, for SW winds. Terrain field subjected to 'Gaussian' attenuation beyond radius R from the origin, with ℓ_d = 40 m or (run D) ℓ_d = 24 m. (b) Terrain perturbation fields over the wide (black) and narrow (red) domains. For results shown on (b) the Gaussian filter, where applied, used terrain damping length ℓ_d = 40 m. (Note: the terrain perturbation is defined relative to average elevation over the computational domain.) (For interpretation of the references to color in this figure legend, the reader is referred to the web version of this article.)

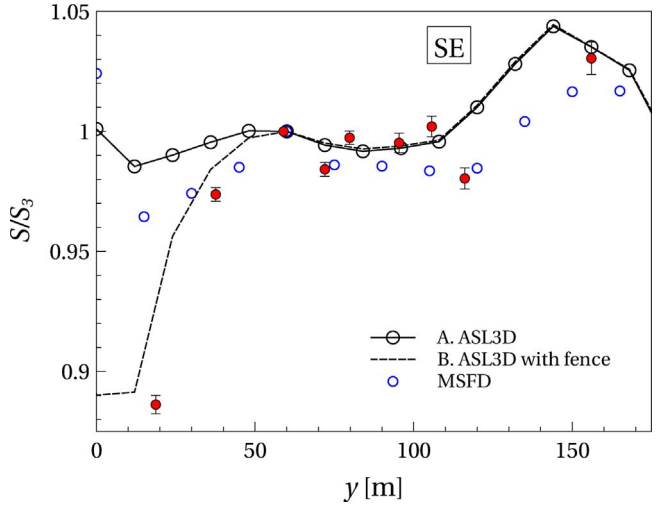

Fig. 9. Measured and modelled transects of mean wind speed in plot 22 at Lacombe, for SE winds. For all simulations the domain spanned (± 960 × ± 960 × 960 m) along respectively the (x, y, η) axes, and the terrain had been subjected to Gaussian attenuation beyond R = 840 m with damping length ℓ_d = 40 m; horizontal resolution for the ASL3D simulations was $\Delta x = \Delta y$ = 12 m. The ASL3D run B designated 'with fence' (dashed line) included a momentum sink representing shelter by the boundary gates and fences along and near y = 0.

plot 22, close to access gates and the boundary fences that ran east–west and north–south through the origin. Additional east–west fences, defining a stock access route and a farm road, lay nearby at $y \sim -5$ m and $y \sim 12$ m and beyond. In case those gates and fences might have

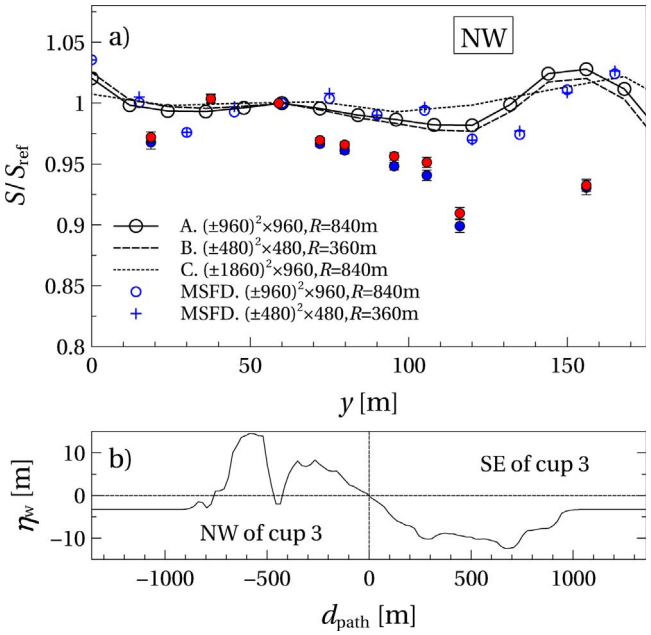

Fig. 10. (a) Measured and modelled transects of mean wind speed in plot 22 at Lacombe, for NW winds. Solid red circles, observed mean transect over runs satisfying $S_{\mathrm{ref}}^{\min} \geq 2.5\ \mathrm{m\ s^{-1}}$ (118 runs); solid blue circles, wind speed threshold increased to $S_{\mathrm{ref}}^{\min} \geq 4.0\ \mathrm{m\ s^{-1}}$ (71 runs). ASL3D simulations A and B used $\Delta x = \Delta y$ = 12 m, while C (on the laterally expansive domain) used $\Delta x = \Delta y$ = 24 m. For all model runs shown, the standard deviation (i.e. damping length) for the 'Gaussian' filter was ℓ_d = 40 m. (b) Transect of *relative* terrain height corresponding to ASL3D simulation A, along a NW–SE line (wind "path") through the reference anemometer (cup no. 3), with negative values lying upwind from anemometer no. 3. (For interpretation of the references to color in this figure legend, the reader is referred to the web version of this article.)

appreciably sheltered cup no. 1, the ASL3D run B simulation included a momentum sink

$$S_v = -k_r V \sqrt{U^2 + V^2}\, \delta(y - 0) s(\eta - h_f) \tag{18}$$

along y = 0 to represent their amalgamated effect (see analogous Eq. (14) for explanation; the momentum sink extended to h_f = 2 m, roughly the height of the fences and gates; the resistance coefficient was prescribed arbitrarily as k_r = 2). The result of adding the momentum sink is a markedly better accord (than seen in the other simulations) with the observations at the south end of the transect.

Turning finally to the case of a NW wind direction, Fig. 10 shows that (as for the NE and SW wind directions) simulations by MSFD and by ASL3D are broadly similar with each other, provided ASL3D is run at adequate resolution ($\Delta x = \Delta y$ = 12 m). However they are not in good accord with the observed wind transects — plural in this case because two transects are shown, corresponding to data selection threshold wind speeds $S_{\mathrm{ref}}^{\min} \geq 2.5\ \mathrm{m\ s^{-1}}$ (118 runs) and $S_{\mathrm{ref}}^{\min} \geq 4.0\ \mathrm{m\ s^{-1}}$ (71 runs).

While disappointing, the poor agreement of the model with the observations for a NW wind direction is not particularly surprising, for it is evident from the terrain contours (Fig. 4) that NW winds present steep and complex topography upwind from plot 22 (there were also woods on that NW slope and at its crest: no attempt was made to represent them). Note too from Fig. 10b that for the NW wind direction the anemometers lay on a lee slope, which is significant because (e.g. Carruthers and Hunt, 1990) in numerical studies broadly similar to the present one "the velocity defect on the lee side of the hill decreased too rapidly on the lee slope." Carruthers and Hunt (see also Weng et al., 1989) adjust the turbulence length scale ("blocking-shear mixing-length model") to try to remedy this, however an approximate implementation of that length scale here, as

$$\frac{1}{\lambda} = \frac{1}{\lambda_0} + \frac{0.6}{\eta} + \frac{\partial\sqrt{U^2 + V^2}/\partial z}{1.3\sqrt{c_e E}}\ , \tag{19}$$

did not appreciably alter the ASL3D transect. Likewise, there was no sign of any qualitative improvement in the solution when (run C in Fig. 10), as a means to mitigate any unwanted consequence of the periodic boundary condition, the domain was expanded to cover almost ± 2 km away from the origin (along x and y), but with the Gaussian filter attenuating the terrain beyond $R = 840$ m — a configuration that provides about a 2 km interlude of flat land that in effect isolates the downwind edge of the (undamped) terrain from the region (upwind) of terrain onset (that is, the wind blows over almost a kilometer of flat land before encountering the outflow boundary, and upon "re-entering" the inflow boundary a further 1 kilometer of flat land before onset of undamped terrain). While this large domain simulation entailed a reduced (and – see also Fig. 7 – evidently inadequate) resolution ($\Delta x = \Delta y = 24$ m) such that the model is unable to resolve the shortest modes (i.e. Fourier components) of the lidar-DEM topography, were the periodic boundary condition responsible for the mediocre simulations at higher resolution the expanded domain should have produced a better model consistency with the longer modes of the wind field — which it did not.

Returning to the fact that Fig. 10 exhibits *two* transects of observed wind speed, and noting the fact that these do not greatly differ, there is a useful point to be made in defense of having treated the model atmosphere as neutrally stratified: for a given magnitude of the vertical heat flux, the increase in threshold wind speed from $S_{\mathrm{ref}}^{\mathrm{min}} \geq 2.5$ m s^{-1} to $S_{\mathrm{ref}}^{\mathrm{min}} \geq 4.0$ m s^{-1} implies a fourfold increase in the magnitude $|L|$ of the Obukhov length, therefore (at all points in the flow) a fourfold reduction in $|\eta/L|$. The absence of any gross change in the transect suggests the influence of stratification on the *selected* data is weak, even when the selection uses the more permissive criterion that $S_{\mathrm{ref}}^{\mathrm{min}} \geq 2.5$ m s^{-1}.

To summarize the performance of ASL3D, given adequate resolution on an adequate domain, Fig. 11 plots model versus observed fractional deviation of mean wind speed from the value at the reference location (i.e. location of cup no. 3), omitting those points at which ASL3D was forced to fit (by the rescaling). The linear correlation coefficient between model and observed values, computed on a sample embracing the best simulation for each wind direction, was a modest 0.72. In short for winds from the NE or SW the models, and more especially so ASL3D, agree quite well with the observations. For SE winds, the model transects show some resemblance to the form of the measured transect, particularly so when (the hypothesized) sheltering by fences is parameterized. However model transects for E or W winds (not shown) were mediocre (cup nos. 1 & 9 standing well away from the models' transect of relative wind speed), while for winds from the NW they exhibited only a weak correlation with the transect observed. As noted above there is reason to consider winds from the NW axis as being intrinsically less amenable to calculation, in view of the steep and wooded terrain lying NW of the anemometers, and the positioning for cup no. 9 in a narrow gulley also presumably challenges the simple modeling paradigm explored here — a paradigm widely reported elsewhere as being more in line with observations on an upslope than on a leeward downslope.

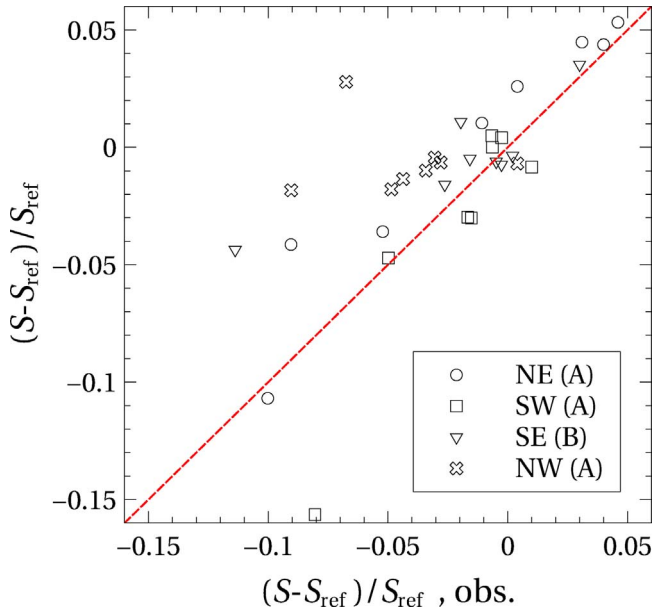

Fig. 11. Modelled (ASL3D) versus observed fractional deviation of mean wind speed from the value at the reference location (i.e. location of cup no. 3). For cross-reference to model transects shown earlier the legend identifies, for each wind direction, the specific ASL3D run plotted. As the wind speeds (observed and modelled) are rescaled to match at the reference location, those points (falling at 0, 0) are not plotted. The linear correlation coefficient between the model and observed data is 0.72.

5. Conclusions

Earliest simulations of the Lacombe wind measurements were made with the pre-existing linear (MSFD) model, and while for the northeast transect agreement with the measurements was at once striking, it was difficult to understand why agreement should be less pleasing for other wind directions – accepting that abrupt topography upwind of the site for northwest winds might mean those cases should be eliminated (as lying outside the legitimate scope of a linear treatment). There was also the question of the disparity near anemometer no. 1. Those puzzles prompted the excursion (here) into the non-linear treatment, which offers, in addition to the retention of non-linear advection, sufficient flexibility to represent drag on fences, allow for stratification, and/or admit (potentially) a resolved grass canopy. That flexibility carries a price: the linear computation completes in seconds to minutes (on an Intel CORE i7 PC), while typically the iterative non-linear code entails hours of calculation.

In regard to the mixed quality of the Lacombe wind simulations of the previous section, the following factors need to be born in mind: (i) the models' imposition of lateral periodicity; (ii) the coarse horizontal resolution (15 m) of the lidar-based Digital Elevation Map; (iii) the assumed uniformity of the shear stress imposed over the upper domain boundary; (iv) the simplicity of the models' $K \propto \lambda\sqrt{E}$ turbulence closure and algebraic lengthscale formulation, and indeed of the RANS approach in its entirety; (v) the imposition of a constant roughness length, and neglect of tree cover along some transect directions; and (vi), the neglect of any influence of Coriolis terms.[5] In addition, recall that each experimental transect is an average over several intervals whose mean wind directions (as observed at a single point in plot 22) fell within a wind direction sector (e.g. 45° ± 22.5° compass angle), such that terrain lying off the nominal or mean wind path would intermittently have lain directly upwind of the anemometers. Only the lateral diffusion terms (parameterized with a small artificial viscosity $K_h^* \sim 0.1$ m^2 s^{-1}) in the numerical model could be said to represent the fluctuation in wind direction, and certainly not with any realism.

Simulations using commercial CFD (Computational Fluid Dynamics) RANS-based codes (such as ANSYS Fluent), though in some respects more sophisticated (e.g. intricate mesh generation, higher-order discretizations for derivatives), would be subject to many of these same limitations. So then, to what extent do the findings of this paper suggest that the wind field *can* be determined over a non-ideal measurement site — as, hypothetically, a means to refine one's representation of the micro-meteorological fields? The imperfection of the suite of simulations shown above, and the fact that they collectively constitute a *band*[6] about the observations, might suggest it would be better to refuse the (impure) site, than depend on a calculation whose fidelity, if these

[5] Neglect of atmospheric stratification has not been added to this list, for it has been argued above that stratification was unimportant for the selected intervals of measurement at Lacombe.

[6] A "band" of simulations rather than a single transect, because quite apart from the arbitrariness implicit in choosing a particular turbulence model (LES or RANS; and with RANS, first- or higher-order closure; and within first-order RANS, one of many possible prescriptions), further subjective choices come into play, such as the domain size, choice of lateral boundary conditions, and the manner of filtering the terrain.

results are indicative, is uncertain. But here a reminder is in order that, absent the model transects and assuming one had not the luxury to expose a large number of anemometers over the site, one has only a *single* datum as regards the wind, at the reference anemometer (in the Lacombe case, cup no. 3): the default situation is that one has only that single measured wind speed such that (of necessity) one would be forced to map that value (unchanged) laterally all over the site, and extrapolate vertically using the appropriate equilibrium wind profile, usually $S(z) \propto \ln(z/z_0)$. Even at their *worst*, these model curves permit an extrapolation no less skillful than to have assumed lateral constancy, while at their best (e.g. Figs. 6–8) the model's mean wind fields are a much superior description than to have invoked lateral homogeneity. Accordingly it seems safe to speculate that, availed of even such a simple three-dimensional representation of the wind field as has been explored here, micrometeorological "applications" such as inverse dispersion (deduction of ground-air emission rates indirectly, from measured concentration rise) should be more robust relative to imperfections of site, than if they were based on the convenient myth of a horizontally-homogeneous wind field. The 'should' is important however, not only because the models' 3D mean wind fields are imperfect, but also because in the context of atmospheric *dispersion* the disturbed field of turbulent kinetic energy is of no less importance than that of the mean wind,[7] and it has long been established that the simple models examined here are less satisfactory in regard to predicting turbulence statistics than as regards the mean wind.

Acknowledgements

The author is grateful to Drs. P.A. Taylor and W. Weng (York University, Ontario, Canada) for having provided the code for MSFD. Funding for this research has been provided by grants from the Agricultural Greenhouse Gases Program of Agriculture and Agrifood Canada and from the Natural Sciences and Engineering Research Council of Canada. Computational support was provided by WestGrid and Compute Canada.

Appendix A. MSFD

The "Mixed Spectral Finite Difference" (MSFD) model of flow over terrain (Beljaars et al., 1987a,b), is founded on a linearization of the momentum equations, in the spirit of Jackson and Hunt (1975), but with height-dependent background velocities. Thus, for example, the U velocity component is decomposed $U = U_0(\eta) + \Delta U(x, y, \eta)$ where ΔU is the flow disturbance (i.e. response to terrain), and advection terms take the form $U_0(\eta)\, \partial \Delta U/\partial x$ (etc). Ayotte et al. (1994) remark that MSFD "assumes a constant stress layer to zero order throughout the vertical extent of the model". The Coriolis terms are neglected, as are gradients in the diagonal components of the Reynolds stresses. As used here, stratification is neutral, and the turbulence closure matches that of the non-linear model (ASL3D, described in Section 2). Thus MSFD is a close cousin of ASL3D: indeed, in the limit of small terrain, there should be little to differentiate the two treatments in terms of fidelity (though much in terms of computational efficiency).

Further details: because MSFD represents the horizontal structure of the wind field by Fourier decomposition, the terrain field is Fourier transformed. MSFD solutions shown here retained 2^n waves with $n = 6$ or 7. It was necessary for the Fourier transform routines of MSFD that there be $2^n + 1$ gridlines along each direction, with the distance interval constrained (by the resolution of the Digital Elevation Map) to be 15 m.

Appendix B. Testing the algebraic core of ASL3D

By 'algebraic core' is meant the "line-by-line" solver ("LBYL"), whose function is to accomplish each refinement ($m \rightarrow m + 1$) of each of the coupled fields that together constitute the numerical solution. Within each such single step or update, LBYL in fact sequentially and *repeatedly* calls two Numerical Recipes subroutines: "cyclic" advances the solution on sweeping horizontal lines of nodes, "tridag" on sweeping vertical lines of nodes. An optional test was coded into the main program (ASL3D), which upon selection used LBYL to solve Laplace's equation $\nabla^2 T = 0$ on a 3-dimensional domain $[-D \le x, y \le D, 0 \le z \le H]$, with lower boundary condition $T(x, y, 0) = 0$, upper boundary condition $T(x, y, H) = \cos(\pi x/D)\cos(\pi y/D)$, and periodic lateral boundary conditions. After an arbitrary number of iterations within LBYL, the numerical solution was compared (statistically and graphically) with the analytical solution, determined as

$$T^{\star}(x, y, z) = \frac{\exp(\sqrt{2}\,\pi\, z/D) - \exp(-\sqrt{2}\,\pi\, z/D)}{\exp(\sqrt{2}\,\pi\, H/D) - \exp(-\sqrt{2}\,\pi\, H/D)} \cos(\pi x/D)\cos(\pi y/D)\ . \tag{20}$$

Table 1 summarizes the results of these tests, in relation to iteration count, choice of first guess field, and gridlength (computational resolution). Computational nodes were uniformly distributed, and results are shown for a 'coarse' grid ($81 \times 81 \times 50$ nodes) and a 'refined' grid ($161 \times 161 \times 98$ nodes) for which discretization error should be much smaller. The mean magnitude of the analytical solution, averaged over all nodes, may be taken as a scale for the root-mean-square solution errors cited in Table 1, values being 9.263×10^{-2} for the coarse grid and 9.067×10^{-2} for the refined grid.

With the first guess taken as $T^{(1)}_{i,j,k} = 0$, which if not the worst possible is at the least a poor start, the solution after (only) 21 iterations was in mediocre accord with the true solution (correlation coefficient[8] 0.935, slope of regression line 0.76). Increasing the iteration count improves the solution, whose accuracy however is compromised by discretisation error and machine roundoff error. If instead the analytical solution $T^{\star}$ is provided as (a perfect) first guess, the numerical solution deteriorates (albeit only slightly) with increasing iteration count, this (again) being attributable to discretization error (the evidence being that, for a given iteration count, the r.m.s. solution error is much smaller on the refined grid than on the coarse grid). Table 1 confirms that the core numerical algebra is performing as it should (a poor solution is progressively improved; a good solution is retained). When applied for the wind calculations, calls to LBYL are repeated while interim states of the solution are nudged progressively towards a converged solution. In view of the manner in which nonlinear terms are evaluated, e.g. U^2 being represented as $U^m U^{m+1}$, it is pointless to seek an extremely accurate solution field at guess $m + 1$ when the prior field U^m is imperfect. For that reason, and because (except initially) the U^m field is usually a good guess for the subsequent solution U^{m+1}, it suffices to terminate iterations of LBYL with a low maximum count, typically 21.

[7] Simply put, the mean wind sets the travel time from source to receptor, while the velocity standard deviations largely control the rate of 'spread' about a nominal plume centreline.
[8] The correlation coefficient was based on the sample of model solution values T^{mod} at all gridpoints and the corresponding sample of true values $T^{\star}$.

Table 1
Diagnostics for solution of Laplace's equation in relation to iteration count, first guess field and computational resolution ($T^{\star}$ is the analytical solution). The mean magnitude of the analytical solution, averaged over all nodes, is 9.263×10^{-2} for the coarse grid, and 9.067×10^{-2} for the fine grid.

1st guess	Grid	Iterations	r.m.s. error	Slope	Corr. coefft.
$T = 0$	Coarse	21	6.58×10^{-2}	0.759	0.935
$T = 0$	Coarse	101	3.91×10^{-2}	0.935	0.975
$T = 0$	Coarse	501	3.85×10^{-2}	0.952	0.976
$T = T^{\star}$	Coarse	21	3.37×10^{-5}	1.00	1.00
$T = T^{\star}$	Coarse	101	6.34×10^{-5}	1.00	1.00
$T = T^{\star}$	Coarse	501	6.79×10^{-5}	1.00	1.00
$T = 0$	Fine	21	1.03×10^{-1}	0.516	0.825
$T = T^{\star}$	Fine	21	2.69×10^{-6}	1.00	1.00
$T = T^{\star}$	Fine	101	8.08×10^{-6}	1.00	1.00

References

Ayotte, K.W., Xu, D., Taylor, P.A., 1994. The impact of turbulence closure schemes on predictions of the mixed spectral finite difference model for flow over topography. Bound. Layer Meteorol 68, 1–33.

Beljaars, A.C.M., Walmsley, J.L., Taylor, P.A., 1987a. A mixed spectral finite-difference model for neutrally stratified boundary-layer flow over roughness changes and topography. Bound. Layer Meteorol. 38, 273–303.

Beljaars, A.C.M., Walmsley, J.L., Taylor, P.A., 1987b. Modelling of turbulence over low hills and varying surface roughness. Bound. Layer Meteorol. 41, 201–215.

Britter, R.E., Hunt, J.C.R., Richards, K.J., 1981. Air flow over a two-dimensional hill: studies of velocity speed-up, roughness effects and turbulence. Q. J. R. Meteorol. Soc. 107, 91–110.

Carruthers, D.J., Hunt, J.C.R., 1990. Fluid Mechanics of Airflow Over Hills: Turbulence, Fluxes, and Waves in the Boundary Layer. In: In: Blumen, W. (Ed.), Meteorological Monographs 23. American Meteorological Society, pp. 83–103 Chapter 5. ISBN 1-878220-01-2.

Castro, F.A., Palma, J.M.L.M., Lopes, A.S., 2003. Simulation of the Askervein flow. Part 1: Reynolds averaged Navier–Stokes equations ($k - \epsilon$ turbulence model). Bound. Layer Meteorol. 107, 501–530.

Doyle, J.D., Epifanio, C.C., Persson, A., Reinecke, P.A., Zängl, G., et al., 2013. Mesoscale modeling over complex terrain: numerical and predictability perspectives. In: Chow, F. (Ed.), Mountain Weather Research and Forecasting. Springer Atmospheric Sciences, pp. 531–589.

Ferziger, J.H., Perić, M., 1997. Computational Methods for Fluid Dynamics. Springer 364pp. ISBN 3-540-59434-5.

Finnigan, J.J., 1988. Air flow over complex terrain. In: Steffen, W.L., Denmead, O.T. (Eds.), Flow and Transport in the Natural Environment: Advances and Applications. Springer-Verlag, pp. 183–229 ISBN 3-540-19452-5.

Golaz, J.-C., Doyle, J.D., Wang, S., 2009. One-way nested large-eddy simulation over the Askervein Hill. J. Adv. Mod. Earth Sci. 1, 1–6.

Hu, N., Flesch, T.K., Wilson, J.D., Baron, V.S., Basarab, J.A., 2016. Refining an inverse dispersion method to quantify gas sources on rolling terrain. Agric. For. Meteorol. 225, 1–7.

Hunt, J.C.R., 1980. Wind over hills. In: Wyngaard, J.C. (Ed.), Workshop on the Planetary Boundary Layer (August 1978, Boulder, Colorado). American Meteorological Society, pp. 107–149 ISBN 0-933876-51-3.

Jackson, P.S., Hunt, J.C.R., 1975. Turbulent wind flow over a low hill. Q. J. R. Meteorol. Soc. 101, 929–955.

Jenkins, G.J., Mason, P.J., Moores, W.H., Sykes, R.I., 1981. Measurements of the flow structure around Ailsa Craig, a steep, three-dimensional, isolated hill. Q. J. R. Meteorol. Soc. 107, 833–851.

Mason, P.J., Sykes, R.I., 1979. Flow over an isolated hill of moderate slope. Q. J. R. Meteorol. Soc. 105, 383–395.

Patankar, S.V., 1980. Numerical Heat Transfer and Fluid Flow. Hemisphere Publ. (McGraw-Hill Book Co.), New York 197pp. ISBN: 0-07-0487404.

Raithby, G.D., Stubley, G.D., Taylor, P.A., 1987. The Askervein hill project: a finite control volume prediction of three-dimensional flows over the hill. Bound. Layer Meteorol. 39, 247–267.

Raupach, M.R., 1989. A practical Lagrangian method for relating scalar concentrations to source distributions in vegetation canopies. Q. J. R. Meteorol. Soc. 115, 609–632.

Richards, K.J., Taylor, P.A., 1981. A numerical model of flow over sand waves in water of finite depth. Geophys. J. R. Astron. Soc. 65, 103–128.

Taylor, P.A., 1977a. Numerical studies of neutrally stratified planetary boundary layer flow above gentle topography. I: Two-dimensional cases. Bound. Layer Meteorol. 12, 37–60.

Taylor, P.A., 1977b. Some numerical studies of surface boundary layer flow above gentle topography. Bound. Layer Meteorol. 11, 439–465.

Taylor, P.A., Walmsley, J.L., Salmon, J.R., 1983a. A simple model of neutrally-stratified boundary-layer flow over real terrain incorporating wavenumber-dependent scaling. Bound. Layer Meteorol. 26, 169–189.

Taylor, P.A., Mickle, R.E., Salmon, J.R., Teunissen, H.W., 1983b. The Kettle's hill experiment – site description and mean flow results. Tech. rept. AQRB-83-002-L. Atmos. Environ. Serv Canada.

Taylor, P.A., Mason, P.J., Bradley, E.F., 1987. Boundary-layer flow over low hills (a review). Bound. Layer Meteorol 39, 107–132.

Taylor, P.A., 1998. Turbulent boundary-layer flow over low and moderate slope hills. J. Wind Eng. Ind. Aerodyn. 74–76, 25–47.

Thomson, D.J., 1987. Criteria for the selection of stochastic models of particle trajectories in turbulent flows. J. Fluid Mech. 180, 529–556.

van Doormaal, J.P., Raithby, G.D., 1984. Enhancements of the SIMPLE method for predicting incompressible fluid flows. Numer. Heat Transfer 7, 147–163.

Versteeg, H.K., Malalasekera, W., 1995. An Introduction to Computational Fluid Dynamics. Prentice Hall 257pp. ISBN 0-582-21884-5.

Weng, W.S., Richards, K.J., Carruthers, D.J., 1989. Some Numerical Studies of Turbulent Wake Over Hills. In: Fernholz, H.H., Fiedler, H.E. (Eds.), Advances in Turbulence 2. Springer, Berlin, Heidelberg, pp. 412–417.

Weng, W., Taylor, P.A., Walmsley, J.L., 2000. Guidelines for airflow over complex terrain: model developments. J. Wind Eng. Ind. Aerodyn. 86, 169–186.

Wilson, J.D., 1985. Numerical studies of flow through a windbreak. J. Wind Eng. Ind. Aerodyn. 21, 119–154.

Wilson, J.D., 2004a. Oblique, stratified winds about a shelter fence. I: Measurements. J. Appl. Meteorol. 43, 1149–1167.

Wilson, J.D., 2004b. Oblique, stratified winds about a shelter fence. II: Comparison of measurements with numerical models. J. Appl. Meteorol. 43, 1392–1409.

Wilson, J.D., Swaters, G.E., Ustina, F., 1990. A perturbation analysis of turbulent flow through a porous barrier. Q. J. R. Meteorol. Soc. 116, 989–1004.

Wilson, J.D., Finnigan, J.J., Raupach, M.R., 1998. A first-order closure for disturbed plant canopy flows, and its application to windflow through a canopy on a ridge. Q. J. R. Meteorol. Soc. 124, 705–732.

Wilson, J.D., Flesch, T.K., Bourdin, P., 2010. Ground-to-air gas emission rate inferred from measured concentration rise within a disturbed atmospheric surface layer. J. Appl. Meteorol. Climatol. 49, 1818–1830.

Wood, N., 2000. Wind flow over complex terrain: a historical perspective and the prospect for large-eddy modelling. Bound. Layer Meteorol. 96, 11–32.

Ying, R., Canuto, V.M., Ypma, R.M., 1994. Numerical simulation of flow data over two-dimensional hills. Bound. Layer Meteorol. 70, 401–427.

Zeman, O., Jensen, N.O., 1987. Modification of turbulence characteristics in flow over hills. Q. J. R. Meteorol. Soc. 113, 55–80.